Characterization of ion-irradiation-induced defects in multi-walled carbon nanotubes

New Journal of Physics
The open-access journal for physics

Characterization of ion-irradiation-induced defects in multi-walled carbon nanotubes

Ossi Lehtinen[1,6], Timur Nikitin[2], Arkady V Krasheninnikov[1,3], Litao Sun[4], Florian Banhart[5], Leonid Khriachtchev[2] and Juhani Keinonen[1]

[1] Department of Physics, University of Helsinki, PO Box 43, FI-00014 University of Helsinki, Finland
[2] Department of Chemistry, University of Helsinki, PO Box 55, FI-00014 University of Helsinki, Finland
[3] Department of Applied Physics, Aalto University, PO Box 1100, FI-00076 Aalto, Finland
[4] Key Laboratory of MEMS of the Ministry of Education, Southeast University, 210018 Nanjing, People's Republic of China
[5] Institut de Physique et Chimie des Matériaux IPCMS-DSI, UMR 7504, 23 rue du Loess, 67034 Strasbourg, France
E-mail: ossi.lehtinen@gmail.com

New Journal of Physics **13** (2011) 073004 (19pp)
Received 22 March 2011
Published 5 July 2011
Online at http://www.njp.org/
doi:10.1088/1367-2630/13/7/073004

Abstract. We study the effects of Ar^+, He^+ and C^+ ion irradiation on multi-walled carbon nanotubes at room and elevated temperatures with transmission electron microscopy (TEM) and Raman spectroscopy. Based on the TEM data, we introduce a universal damage scale for the visual analysis and characterization of irradiated nanotubes. We show for the first time that the amount of irradiation-induced damage in nanotubes is larger than the value predicted for bulk materials using the simple binary collision approximation, which may be associated with higher defect production due to electronic stopping in these nanoscale systems. The Raman spectra of the irradiated samples are in qualitative agreement with the TEM data and indicate the presence of irradiation-induced defects. However, it is difficult to obtain quantitative information on defect concentration due to non-uniform distribution of defects in the nanotube films and in part due to the presence of other carbon nanosystems in the samples, such as graphitic crystallites and carbon onions.

[6] Author to whom any correspondence should be addressed.

Contents

1. Introduction

The inevitable presence of atomic-scale defects in carbon nanotubes is responsible for the substantial difference between their theoretically predicted and experimentally measured mechanical and electronic properties [1]. Defects typically have detrimental effects on the characteristics of nanotubes. For example, they lead to the measured [2] values of tensile strength being much lower than those theoretically predicted [3, 4] and higher electrical resistivity [5, 6]. However, defects can also be useful, as they can give rise to enhanced field emission [7, 8] and mechanical strengthening of nanotube bundles [9, 10], multi-walled nanotubes (MWCNTs) [11] and bulk nanotube samples [12–14]. Moreover, the intentional introduction of defects into carbon nanotubes by irradiation has recently been demonstrated to be a powerful tool for engineering the atomic and electronic structures of nanotubes and graphene [15, 16].

Research on irradiation effects in carbon nanosystems has been motivated not only by practical aspects of materials processing or the requirement to know the behavior of nanotubes in radiation-hostile environments, such as outer space, but also by the fundamental aspects of understanding the response of such low-dimensional systems to irradiation. Indeed, many fascinating irradiation-induced phenomena in carbon nanomaterials inherently related to their nanometer size have been reported, for example, pressure build-up inside irradiated carbon onions [17–19] and nanotubes [20, 21]. Moreover, small-dose ion irradiation has been demonstrated to result in ordering of fullerene and carbon nanotube films [22], while electron irradiation gives rise to an increase in nanotube film conductance [12, 23, 24].

Complete understanding of irradiation effects in carbon nanomaterials is not possible without a careful characterization of defects. Several experimental techniques can be used to detect irradiation-induced changes in nanoscale carbon materials: for example, Raman spectroscopy [25–28], x-ray photo-electron spectroscopy [29–32] and the electron spin resonance method [33, 34]. Among them, Raman spectroscopy is the most widely used tool,

as this non-destructive method enables one to quickly assess the overall number of defects in a sample or even in individual nanotubes [27]. Moreover, it has been used to obtain quantitative information on the number of defects induced by low-energy (90 eV) ion irradiation on single and multi-layer graphene [35, 36]. However, as we show below, quantitative analysis of the defect concentration in nanotube films is a non-trivial task.

In this work, we combine transmission electron microscopy (TEM) and Raman spectroscopy to study the relationship between defect concentration in films of nanotubes and the Raman spectra. MWCNTs were irradiated with Ar^+, He^+ and C^+ ions with a wide range of irradiation energies and fluences and at different temperatures. The samples were characterized using TEM and Raman spectroscopy. We use TEM as the main tool for analyzing ion irradiation damage in MWCNTs. To facilitate visual analysis of the TEM images of the irradiated MWCNTs, we introduce a damage grade scale, where the damage is mapped on a scale from 0 to 5, with 0 being a perfect undamaged specimen and 5 being a completely amorphous carbon nanorod. We demonstrate that the use of Raman spectroscopy for measuring irradiation damage in bulk nanotube samples is not straightforward. This problem, related to non-uniform distribution of damage, is studied in detail.

2. Experimental

2.1. Materials

The samples used in the high-resolution TEM study were purified arc discharge MWCNTs deposited on molybdenum TEM grids (except for sample 'm' in table 1, where a copper grid with markings was used to assist in locating the same nanotube before and after the ion irradiation). In addition to nanotubes, the samples contained a considerable number of carbon onions and graphitic crystallites, but not much amorphous carbon. This material is referred to as material A below. The material was first dispersed in a solvent through sonication, and a droplet of the dispersion was deposited on a grid. This results in a solid layer of varying thickness on the grid. Thin enough areas down to individual tubes can be located in the samples for TEM analysis. For Raman measurements, we used places on the grid with maximal thickness of the material. These spots are clearly visible to the eye; thus, the thickness in these areas is presumably about 1 μm. We also studied another material, referred to as material B. This material, made out of so-called bamboo MWCNTs, was produced by a commercial vendor (NanoLab Inc., USA) and was supplied in the form of a paper-like sheet (also called buckypaper) with a density of approximately 0.5 g cm^{-3}. As a reference, we studied the effects of irradiation on graphite. The samples were polycrystalline graphite cut into approximately 2 mm-thick pieces, which were mechanically polished to a smooth surface.

2.2. Ion irradiation

Ion irradiation was conducted using a 500 kV ion implanter system manufactured by High Voltage Engineering Europa BW. The ions were produced in a cold cathode Penning ion source from gas phase materials. An analyzing magnet was used to separate the desired mass-to-charge state ratio from a mixture of ions produced in the ion source. The stream of ions was then directed into an electric field generated by a solid state multi-doubler stack of 0–500 kV and thus accelerated into an energetic ion beam. Various magnetic and electrostatic ion optical

Table 1. Summary of the irradiation parameters for the samples presented in figure 2. The energies are given in keV, and ϕ stands for irradiation fluence, i for irradiation current density, RT for room temperature and DG for damage grade. S_n and S_e stand for nuclear and electronic stopping power, respectively, in graphite and are given in units of keV nm^{-1} and are specific to the given ion–energy combinations. dpa is the number of times an atom has been displaced at the depth of 15 nm as calculated by TRIM [44].

Sample	Ion	E	ϕ (1 cm^{-2})	i (μA cm^{-2})	T (°C)	DG	S_n	S_e	dpa
a	Ar^+	40	2.2×10^{14}	0.5	RT	2	0.75	0.41	0.14
b	Ar^+	40	5.5×10^{14}	0.5	RT	3	0.75	0.41	0.36
c	Ar^+	40	1.1×10^{15}	0.5	RT	4	0.75	0.41	0.72
d	Ar^+	40	5.5×10^{15}	0.5	RT	5	0.75	0.41	3.6
e	Ar^+	40	5.5×10^{15}	2	150	5	0.75	0.41	3.6
f	Ar^+	40	5.5×10^{15}	1	300	3	0.75	0.41	3.6
g	Ar^+	40	5.5×10^{15}	2	600	2	0.75	0.41	3.6
h	He^+	350	1.4×10^{17}	4	RT	3	0.0011	0.41	0.033
i	He^+	50	7.1×10^{16}	5	500	1	0.0052	0.21	0.31
j	He^+	50	7.1×10^{17}	5	500	1	0.0052	0.21	3.1
k	C^+	30	1.0×10^{15}	2	RT	2	0.10	0.30	0.11
l	C^+	30	1.0×10^{15}	2	800	0	0.10	0.30	0.11
m	C^+	380	1.0×10^{17}	1	500	3	0.020	0.79	1.34

instruments were used along the beam line to ensure the focusing and correct alignment of the ion beam. The focused ion beam was then run through a beam sweeping system, which rasters the beam across a desired area, resulting in homogeneous exposure at the target. Faraday cups with a known cross-section were placed inside the exposed area and the accumulated charge was measured, from which the number of ion impacts per unit area could be determined. The whole system was in vacuum of $\sim 10^{-7}$ mbar. The vacuum was maintained using turbomolecular high-vacuum pumps assisted by rotary vane and scroll pumps.

The sample was mounted inside a copper pellet with a cavity in the center, and the pellet was clamped onto a larger copper heating stage for high-temperature irradiation. The temperature was measured from the heating stage at the point where the pellet was clamped. As the ion beam may heat the target, depending on the current intensity, and radiative cooling may lower the temperature of the nanotubes, the temperatures given in table 1 should be considered as estimates.

2.3. Transmission electron microscopy

The samples were examined in a high-resolution TEM (FEI Tecnai F-30) with a field emission gun and an acceleration voltage of 300 kV before and after ion irradiation. The electron irradiation dose was kept as low as possible to minimize the effects of electron irradiation.

It is worth noting that as the ion irradiation and TEM were performed from the normal direction of the TEM grids, it can safely be assumed that the samples seen in the TEM images were directly exposed to the ion irradiation and were not shielded by, e.g., other nanotubes on the grid.

2.4. Raman spectroscopy

The Raman spectra were recorded with two setups due to historical reasons. The first setup consists of an Ar ion laser (514.5 nm, Omnichrome 543-AP), a single-stage spectrometer (Acton SpectraPro 500I, resolution 3 cm^{-1}) and a CCD camera (Andor InstaSpec IV). The laser beam was focused to a spot of about 40 μm. Raman spectra were also recorded with a LabRam confocal microscope (HR 800 Jobin Yvon) using excitation at 488 nm of an Ar ion laser (<0.5 mW on sample), 50× and 100× objectives and spectral resolution 2 cm^{-1}. This equipment has been recently used for the successful characterization of single-walled carbon nanotubes [37].

3. Universal damage grade

When probing a large parameter space (e.g. in ion irradiation experiments one can alter the ion species, energy and fluence, temperature, etc) using a TEM, one quickly accumulates a large number of images and quantifying the response of the target material to the treatments becomes increasingly difficult without a general point of reference. This problem is present also when results reported in different papers are to be compared.

The typical features in TEM images of defective MWCNTs are the average length of uninterrupted wall segments and the overall degree of amorphization. The apparent discontinuities originate from dislocations in graphitic sheets [38], defect clusters and completely broken shells. These structures are normally formed due to agglomerations of point defects [39–41], such as vacancies and interstitials. The latter likely form di-interstitials, which are normally embedded into graphitic shells [42] without any under-coordinated atoms forming the so-called inverse Stone–Wales defects [43] and giving rise to additional local curvature. Based on these features, a universal scale can be constructed, which can be used to classify the condition of an MWCNT after a specific treatment, which in turn facilitates more direct comparison of the effects of different treatments.

Such a scale is proposed in figure 1. The table defines a numerical damage grade of MWCNTs ranging from 0 for a perfect undamaged nanotube to 5 for a completely amorphized nanorod. Example TEM images are presented for six steps in the scale along with a short description of characteristic features.

When utilizing the scale, a TEM image of a sample is compared to the damage grade table and a damage grade is assigned. Below, this damage scale is employed when analyzing TEM images of MWCNTs after various irradiation treatments. In this usage case, the scale is of great help when comparing the effects of the treatments.

4. Effects of ion irradiation on the structure of multi-walled nanotubes

4.1. Transmission electron microscopy analysis of ion irradiation effects

In the present study, MWCNT samples made out of material A were irradiated using the parameters tabulated in table 1. Each of the samples was imaged using TEM in order to assess their condition after the irradiation treatment. Also, a damage grade was assigned to each of the samples and the assigned values are listed in the table.

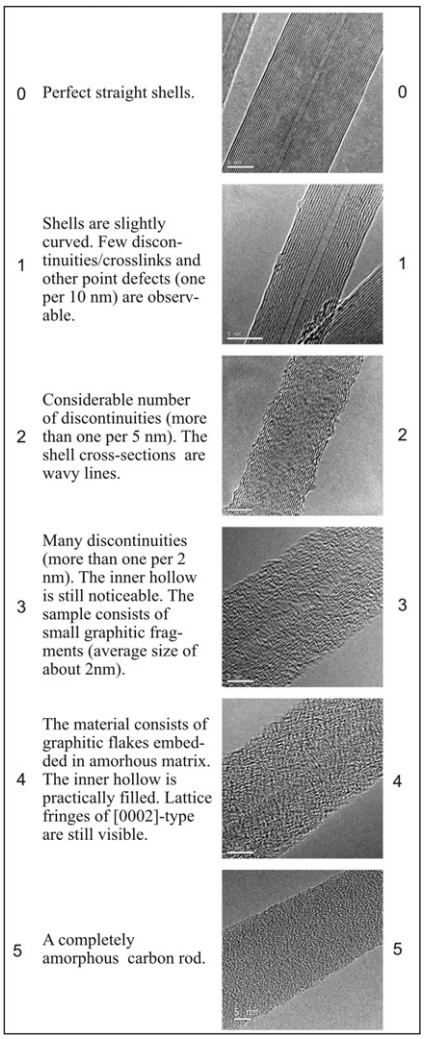

Figure 1. Universal damage grade table for visual analysis and comparison of TEM images of multi-walled carbon nanotubes with defects.

In figure 2, typical TEM images of the samples tabulated in table 1 are presented. In panels (a)–(d), images of samples irradiated with the same ion species (Ar) and energy (40 keV) at room temperature but with gradually increasing total fluences are shown. A clear progressive increase in damage can be observed. Sample (a) exhibits a regular structure after the irradiation, while the level of damage gradually increases in samples (b) and (c), ending in a completely amorphous sample (d).

The influence of sample temperature on the response of nanotubes to ion irradiation can be observed in figures 2(d)–(g). The samples shown in these panels were all irradiated with 40 keV Ar^+, similarly to the previous samples. Irradiation fluence was kept constant, and the parameter varied was the temperature of the target. The samples irradiated at room temperature as well as at 150 °C became completely amorphous, but as the sample temperature was increased to 300 °C and higher, the final damage level of the sample was considerably lower. This is well in line with previous experimental and theoretical results [45, 46] on the behaviour of nanotubes under electron irradiation at elevated temperatures, where self-healing of nanotubes due to vacancy

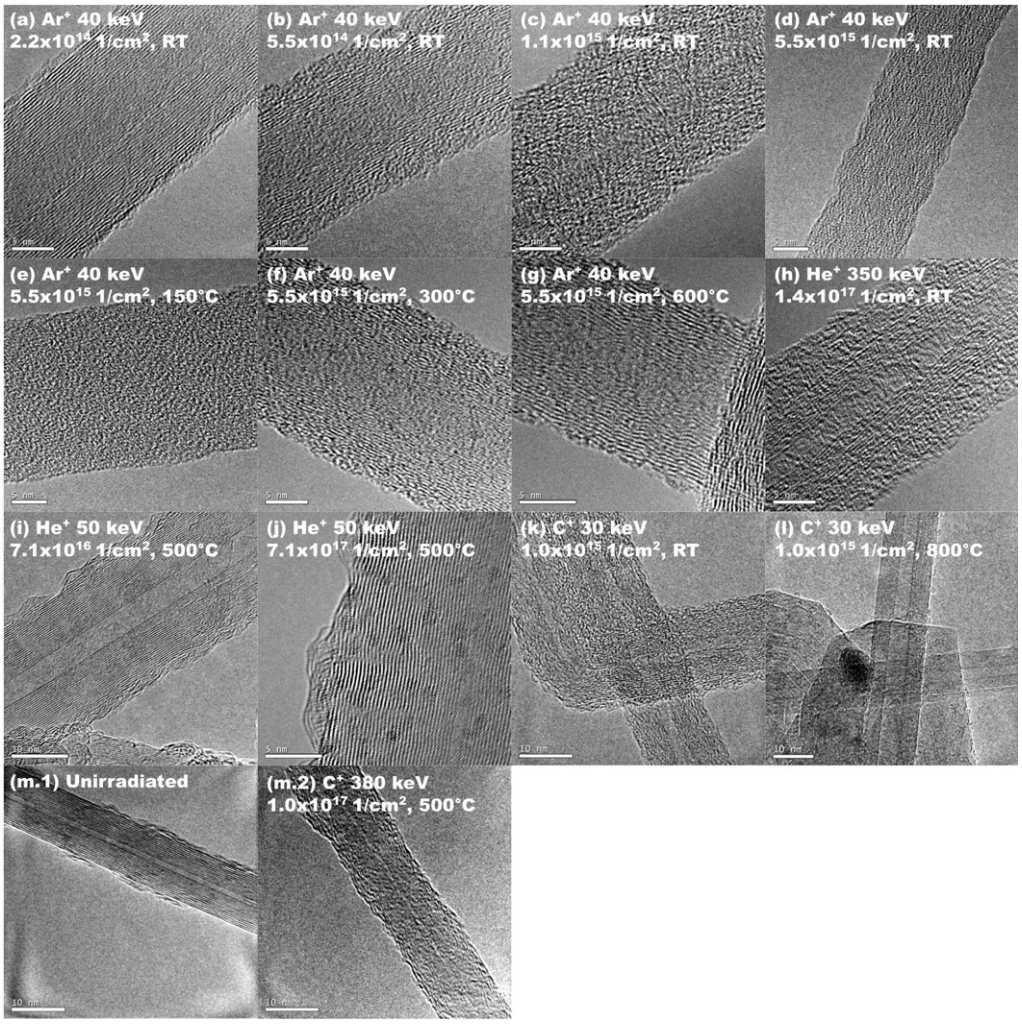

Figure 2. Transmission electron microscope images of multi-walled carbon nanotubes irradiated with different ion species, energies and fluences at varying sample temperature. (a–d) The progression of damage under irradiation with an increasing fluence of 40 keV Ar^+. (d–g) The influence of elevated temperature on the ion irradiation response of an MWCNT. (h) Damage generated predominantly through electronic stopping. (i–l) The effects of elevated temperature. (m.1, m.2) The same nanotube before and after ion irradiation.

migration and coalescence [47] starts at approximately 300 °C. Recombination of Frenkel pairs, stimulated mostly by the migration of adatoms [48] and interstitials bound to the shells as in graphite [49–53], contributes as well. Note that the interstitials in the inner hollow of the nanotubes are highly mobile already at room temperature [45], but this process is not sufficient for efficient self-healing.

In figure 2(h), a sample irradiated with 350 keV He^+ at room temperature is shown. The irradiation fluence was two orders of magnitude higher than that of any of the preceding Ar^+ irradiations. As is to be expected from the considerably smaller displacement cross-section for

lighter He^+ as compared to Ar^+ in carbon nanomaterials [54, 55], an MWCNT can withstand a much higher fluence of He^+ irradiation compared to Ar^+ irradiation. One gets comparable grades of damage with 40 keV Ar^+ irradiation with a fluence of 5.5×10^{14} ions cm^{-2} and with 350 keV He^+ with a fluence of 1.4×10^{17} ions cm^{-2}.

In figures 2(i) and (j), two samples irradiated with 50 keV He^+ at an elevated temperature of 500 °C and two different fluences (7.1×10^{16} and 7.1×10^{17} ions cm^{-2}) are displayed. Both of the samples are only slightly damaged, with more discontinuities in the shells of the sample with higher fluence. Comparing these samples to the sample in panel (h), a sharp difference in irradiation resilience can be observed. The considerably lower damage grade compared to what could be expected from the estimated dpa values can be explained by the self-healing behaviour at elevated temperatures.

In figures 2(k) and (l), two samples irradiated with 30 keV C^+ and similar fluences but at different temperatures are shown. Here again, the effect of *in situ* annealing is evident, as the sample irradiated at elevated temperature is in considerably better condition than is the sample irradiated at room temperature. Finally, in panels (m.1) and (m.2), the condition of the same MWCNT is shown before and after irradiation with 380 keV C^+ at a temperature of 500 °C. These images confirm that the damage we observe is, in fact, ion-irradiation-induced and not, for example, due to the MWCNTs being originally defective.

Using the proposed universal damage scale, comparison of the irradiated samples is straightforward. If, for example, one examines all irradiation parameters that lead to midrange (2–3) damage level (samples a, b, f, g, k and m), one can directly assess the resilience of the MWCNTs under these treatments. Moving from 40 keV Ar^+ (a) to lighter 30 keV C^+ (k) more than doubles the fluence, leading to a similar level of damage in the tube. Increasing the sample temperature to >300 °C gives an order of magnitude improvement in resilience (samples b, f and g). Increasing C^+ energy to 380 keV from 30 keV combined with elevated temperature enables the nanotube to withstand a fluence two orders of magnitude higher (samples k and m). These cases by no means provide a comprehensive picture of ion irradiation effects in MWCNTs, but do provide points of reference to the ion irradiation response.

4.2. Damage production mechanisms

Matter absorbs energy from energetic ions passing through it, which is generally referred to as stopping power, which can be divided into two parts: nuclear and electronic stopping [56]. In the case of nuclear stopping, energy is transferred through elastic collisions with the target atoms. In the case of electronic stopping, energy is transferred through inelastic interactions with the target electrons. Both mechanisms can lead to the production of damage in the target. Elastic collisions lead directly to displacements of the target atoms and possible collision cascades, as the displaced atoms themselves hit the surrounding atoms. The detailed mechanism through which electronic stopping leads to damage in materials is not fully understood to date. However, rapid melting and subsequent cooling of materials due to coupling of the excited electrons and phonons have been suggested as the main avenue of damage production in conducting materials [57]. Graphite has been experimentally [58] and theoretically [59] shown to be quite resistant to damage creation through electronic stopping. A lower limit of ~ 7 keV nm^{-1} in electronic stopping has been measured under which no damage is created in graphite, attributed to graphite's good heat and charge conduction.

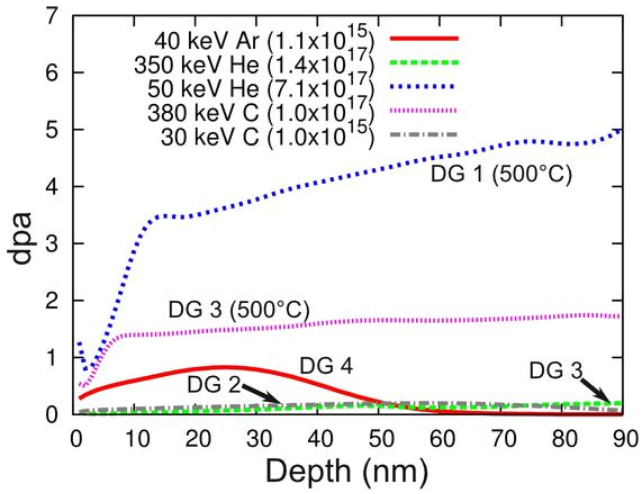

Figure 3. The dpa profiles resulting from the irradiation, as estimated by the TRIM code [44] that calculates the number of displacements using the binary collision approximation, ignoring the contribution of electronic excitations. The dpa value describes how many times an atom has been displaced on average from its original position. The DG markings indicate the damage grade after each of the irradiation treatments based on TEM images (elevated temperatures are shown in parentheses).

Stopping powers for the ions used are shown in table 1, calculated as described in [56], where the nuclear stopping estimate is based on the binary collision approximation of screened nuclei and the electronic stopping estimate on a model fitted to a large number of experimental data. Additionally, numerical Monte Carlo simulations were run in order to estimate the amount of damage created by the ions, using the TRIM code [44]. These simulations are based on calculating the binary collisions of ions and recoiled atoms moving in amorphous material and they essentially model damage creation related to nuclear stopping. This is a standard way of estimating ion irradiation damage, although damage may be overestimated in nanoscale targets [60]. Figure 3 shows displacements-per-atom (dpa: the average times each target atom has been displaced) profiles in graphite after selected irradiation treatments along with assigned damage grades based on the TEM images. Additionally, dpa values at the depth of 15 nm are presented in table 1.

It is not straightforward to deduce which dpa value would lead to what kind of damage level in an MWCNT, since the displaced atoms can recombine with vacancies, larger-scale reconstructions of damaged parts can take place and, especially in the case of high level of damage, atoms displaced once already can be displaced again. Still, the dpa value can be used as a measure of the relative amount of damage originating from nuclear collisions. The samples irradiated at room temperature (samples a, b, c, d, h and k) are most relevant for this treatment, as the *in situ* annealing of defects at high temperatures further obscures the connection between the dpa values and observed levels of damage.

If samples a and k, which both have the same damage grade of 2, are compared, the dpa values seem to match well (0.14 and 0.11). However, if samples b and h are compared, a large difference can be observed in the dpa values (0.36 and 0.033) although the damage

grade of the nanotubes is similar. This indicates that the produced damage cannot be explained with elastic collisions only. On the other hand, the electronic stopping values for all cases are much lower than the 7 keV nm^{-1} limit, below which no damage is created in graphite. This can be interpreted as MWCNTs being more susceptible to damage through electronic stopping than is bulk graphite. The reason for this could be the one-dimensionality of a nanotube, as heat and electronic excitations have much fewer routes to dissipate than in bulk [16]. Further, all of the shells of MWCNTs are not necessarily metallic conductors [1] and defects reduce the conductivity further [5, 6] (although very low defect concentrations have been reported to slightly decrease the resistivity of bulk graphitic samples [61] and single-walled nanotube buckypaper [13]), and semi-conductors and insulators are known to typically have lower thresholds of electronic stopping for damage production [62].

5. Raman spectra and discussion

Defect-induced changes in Raman spectra of carbon materials have been extensively studied (see e.g. [27, 35, 36, 63, 64]). In Raman spectra of single crystal graphite as well as defect-free carbon nanotubes, a peak is observed at approximately $\sim$1580 cm^{-1}, which is commonly referred to as the G band [25]. If imperfections are introduced into graphitic planes, another peak appears at approximately $\sim$1350 cm^{-1} (the D band, where 'D' stands for disorder). The intensity ratio of the D and G bands depends on the size of graphitic in-plane crystallites and hence this ratio has been widely used to characterize the perfection of various carbon materials [65, 66]. Although the ratio is a non-monotonic function of defect concentration (after a natural initial increase with the number of defects, it decreases again when structural defects in the sp^2-hybridized carbon matrix overlap [35, 36, 63]), for some systems (e.g. graphene) Raman spectroscopy can be used to obtain quantitative information [35, 36] on the number of defects in the sample.

Figure 4(a) shows a low-resolution TEM picture of material A (good-quality nanotubes with carbon inclusions deposited on TEM grids). A Raman spectrum from this material is represented by the upper trace in figure 4. It consists of a strong G band with a very weak D band. This spectrum shows that the pristine material consists of an essentially unperturbed sp^2 coordinated carbon network. A similar Raman spectrum for pristine nanotubes was reported by Mathew *et al* [67]. The amount of amorphous carbon is small in the pristine material. On the other hand, it is practically impossible to distinguish between Raman contributions from nanotubes, crystalline grains and other carbon impurities seen in the TEM image. Upon irradiation with Ar^+, the D band grows and both D and G bands become broad, which indicates ion-irradiation-induced disorder. This trend is what can be expected in these experiments. However, the quantitative progress of Ar^+-irradiation-induced changes is in disagreement with the results of [68], where the irradiation effect was much smaller (different sample thicknesses may contribute here, as discussed below). Our Raman spectrum consists of very broad D and G bands that are typical of amorphous carbon, possibly with some amount of sp^3 bonded network [66]. When ion irradiation is performed at elevated temperatures, the change of Raman spectra, and hence the structure, is less pronounced, which indicates that *in situ* annealing reduces the accumulated damage, and this qualitatively agrees with the TEM data presented in table 1. However, we should admit that it is very difficult to establish a straightforward correlation between damage in individual nanotubes and the 'integrated' Raman spectrum. The first complication arises from contamination of samples (see figure 4(a)) because

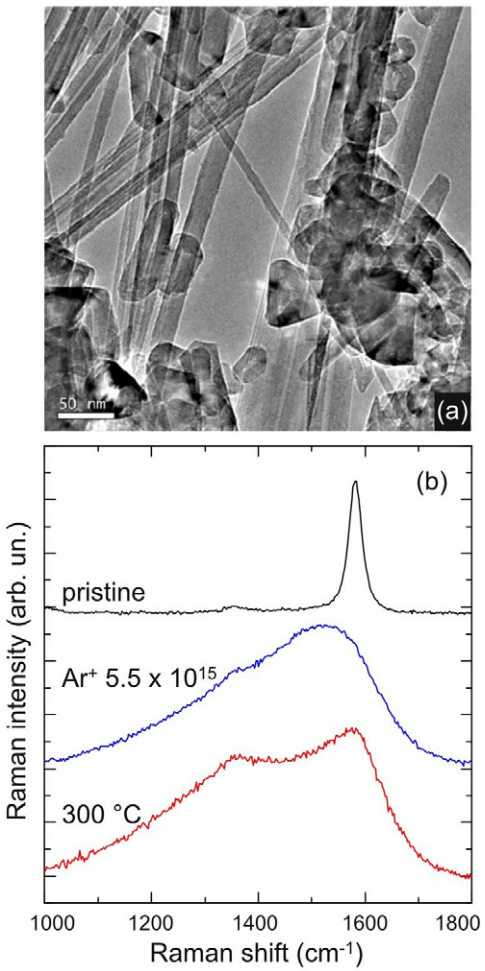

Figure 4. (a) TEM image of material A. (b) Raman spectra obtained from the pristine sample and after irradiation with 40 keV Ar^+ at room temperature and 300 °C.

the contribution of the different structures in the Raman spectrum cannot be distinguished. Moreover, the Raman scattering cross-sections of various phases differ, and they undergo different changes upon ion irradiation. Further on, due to the limited penetration depth of the ions, a contribution from non-irradiated parts of the sample material can be present in the spectra.

Material B (bamboo-type nanotubes in the form of buckypaper) substantially differs from material A at various scales (cf the material morphologies shown in figures 4(a) and 5(a)). On the one hand, material B has fewer large impurities like graphitic crystallites. On the other hand, the structure of individual tubes is less regular than in material A. The Raman spectrum of the pristine material B (the upper trace in figure 5(b)) clearly reflects this difference as the D band is relatively strong, indicating numerous defects in the sp^2 bonded carbon. A similar Raman spectrum of pristine carbon nanotubes was reported by Ni *et al* [68] and by Nichols *et al* [69]. Remarkably, the Raman spectra of the thick layers of material B undergo much smaller ion-irradiation-induced modifications than those obtained for material A. In fact, these changes are weaker than those reported by Ni *et al* after a similar irradiation treatment [68].

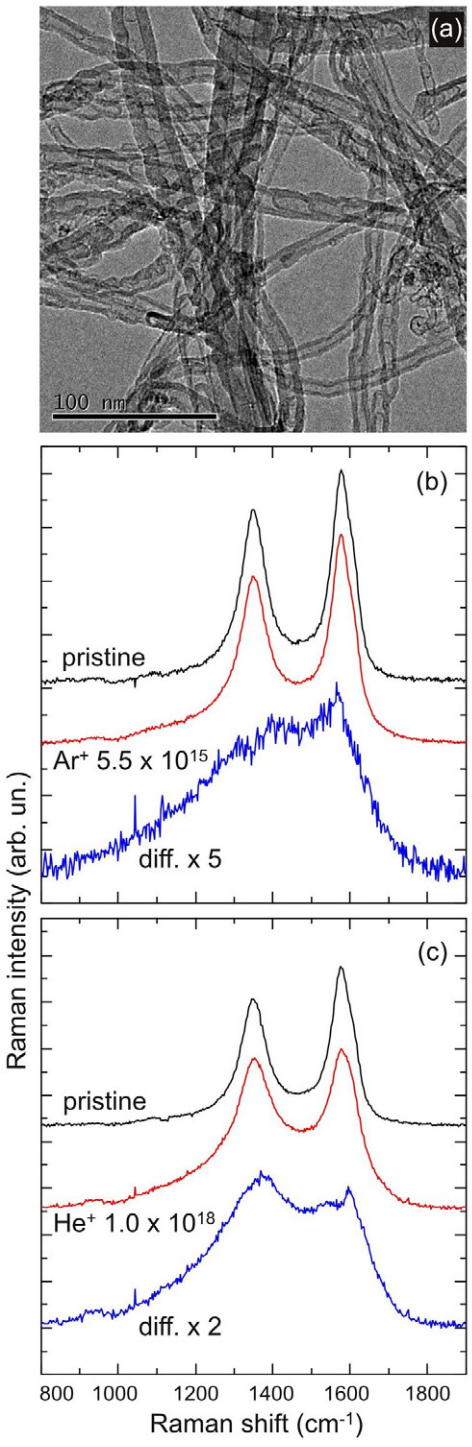

Figure 5. (a) TEM image of material B. (b) Raman spectra of the pristine sample and measured after irradiation with 40 keV Ar^+ at room temperature. The lower curve shows the difference between the two upper spectra. (c) Raman spectra obtained from the pristine sample and after irradiation with 350 keV He^+ at room temperature. The lower curve shows the difference between the two upper spectra.

The spectrum of material B after irradiation seems to consist of two parts: signals from unperturbed tubes and from a highly defective material (of course, this separation is approximate due to the presence of intermediate structures). This concept is demonstrated by the lowest spectrum in figure 5(b), which presents the difference of the two upper spectra taken in appropriate proportion. The obtained difference spectrum is quite similar to that measured after Ar^+ irradiation of material A, and this broad spectrum develops under irradiation. Thus, the material probed by Raman spectroscopy roughly has two spatial parts, perturbed and unperturbed by ions. This fact finds a straightforward explanation in terms of penetration of ions and photons into a solid material. Our calculations (the depth axis should be scaled by a factor of four in figure 3 to take into account the reduced density) estimate the penetration depth of 40 keV Ar^+ as about 200 nm for the carbon material with 25% mass density of graphite. The effective thickness probed by Raman spectroscopy is $1/2\alpha$, where $\alpha = 4\pi k/\lambda$ is the absorption coefficient (k is the extinction coefficient and λ is the laser wavelength) [70]. Taking $k = 0.175$, which is 1/4 of the extinction coefficient of glassy carbon [71] (if k is assumed to scale linearly with density), we obtain 250 nm as the effective thickness of Raman probing, which seemingly matches well with the ion penetration depth. However, the absorption coefficient most probably decreases upon ion-irradiation-induced amorphization of the material. The absorption of amorphous carbon (essentially sp^2 coordinated) is several times less than that of glassy carbon [66]. Moreover, the Raman scattering cross-section and absorption may decrease upon ion irradiation if an sp^3 fraction is produced. Thus, we conclude that Raman spectroscopy effectively probes the material in deep areas that are not damaged by the 40 keV Ar^+ ions. These estimates are in agreement with the spectra shown in figure 5(b). This can also explain at least partially the differences between the spectra from material A and the spectra from material B since the samples of material B are thicker as compared to the samples of material A, leading to a stronger contribution from the deeper (undamaged) areas.

The experiments with He^+ irradiation of the same material B are in agreement with the proposed model (figure 5(c)). According to our calculations, irradiation with He^+ produces about 1 dpa in the bulk, whereas the previous irradiation with Ar^+ led to substantially higher dpa values. However, the Raman spectra of the sample irradiated with He^+ indicates more damage as compared to the Ar^+ irradiation. This fact can be explained by the much deeper penetration of He^+ into the material. The range of He^+ with such energy is much longer than that of photons (average range of the ions is $\sim 5\,\mu$m). On the other hand, dpa is much less than 1 in the first 200 nm of the material (see figure 3), which can explain the incomplete amorphization indicated by the Raman spectra. However, one should note that dpa does not seem to fully describe the produced damage due to the contribution of electronic-stopping-induced damage, as discussed above.

We further studied the effect of ion penetration depth on the Raman spectra. As mentioned above, the analysis of Raman spectra from samples with non-uniform defect distribution is not straightforward. To confirm this, three polycrystalline graphite and nanotube samples (material B) were irradiated with Ar^+ in a specific manner. The ion energies and fluences were selected in such a way that each of the samples had approximately the same number of vacancies (as estimated by TRIM [44]), but with different spatial distributions. Sample 1 was irradiated with Ar^+ with a kinetic energy of 400 keV and a fluence of 4.4×10^{13} ions cm^{-2}, which results in a wide peak located at approximately 300 nm in a graphite sample (approximately four times deeper in the nanotube sample, due to the lower density). Sample 2 was irradiated with Ar^+ with multiple energies and fluences selected to produce a nearly uniform defect distribution up to the

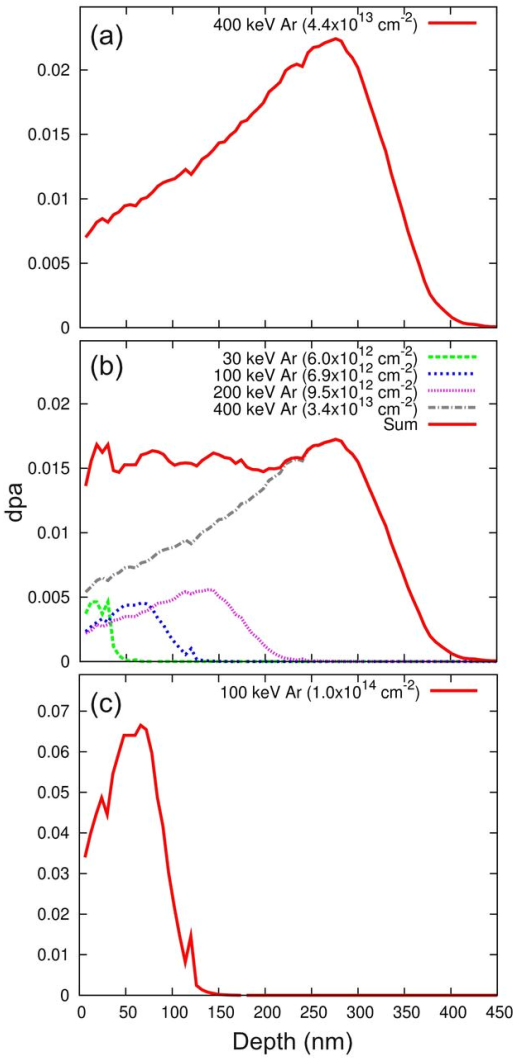

Figure 6. Estimated displacement per atom profiles for the three graphite samples calculated with the computer program TRIM [44]. The first sample has a wide defect profile with a peak at approximately 300 nm. The second sample was irradiated with ions of different energies, resulting in close to uniform damage distribution up to 300 nm. The third sample has a narrower damage peak close to the sample surface. Note the different y-scale in the last graph.

depth of 300 nm and sample 3 with 100 keV Ar^+ and a fluence of 1.0×10^{14} ions cm^{-2}, resulting in a narrower peak at 50 nm (in graphite). The estimated dpa profiles are shown in figure 6 for each graphite sample. Note that the areas under each curve in figure 6 are approximately the same. For the CNT samples, the calculations give the same result with the accuracy of the sample density.

The Raman spectra of these samples are presented in figure 7. The spectra show clear differences, although the total number of defects is similar in these three samples and only the spatial distribution is varied. The spectrum obtained from sample 1 is closer to the spectrum from the pristine sample compared to the others. This indicates that Raman spectroscopy does

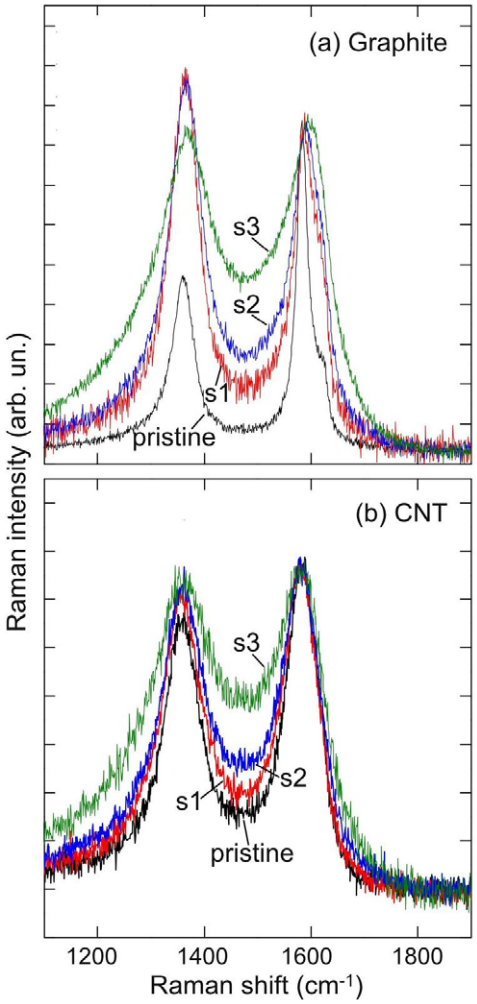

Figure 7. Raman spectra of the pristine samples and those after irradiation with Ar^+ (samples 1, 2 and 3 with dpa profiles shown in figure 6) from (a) graphite and (b) nanotubes (material B).

not probe the deep bulk damaged by 400 keV Ar^+. More damage is located near the surface layer in sample 2; consequently, the measured Raman spectrum indicates more disorder in this sample. The spectrum from sample 3 indicates the highest level of damage as the damage is concentrated closer to the surface, where Raman probing is most effective. Thus, it is impossible to deduce quantitative information on the damage without *a priori* knowledge of the irradiation effects.

6. Conclusions

In this work, TEM images and Raman spectra of multi-walled carbon nanotubes irradiated with Ar^+, He^+ and C^+ ions with various energies, fluences and at different sample temperatures have been studied. The degree of amorphization of MWCNTs after irradiation with the different ions and fluences was assessed from the TEM images. The Raman spectra displayed qualitatively

similar trends, giving support for the TEM results. Elevated temperature of 300 °C or higher increases the resilience of MWCNTs under ion irradiation due to efficient *in situ* annealing of the irradiation-induced defects. To assist visual analysis of TEM images of irradiated MWCNTs, we introduced a universal damage grade scale, where the damage is mapped on a scale from 0 to 5, with 0 representing a perfect undamaged specimen and grade 5 corresponding to a completely amorphous carbon nanorod (figure 1). Such a scale can be useful when comparing the structure of carbon nanotubes irradiated using different irradiation parameters.

We have shown for the first time that the amount of ion-irradiation-induced damage in MWCNTs can be higher than predicted by taking only elastic collisions of the ion and target atoms into account. This may be associated with electronic excitations and the reduced dimensionality of such systems, which affects the dissipation of energy brought in by the ion. This could facilitate the production of defects at lower levels of electronic stopping power than in bulk systems. However, our results do not provide unambiguous evidence for that, and further experiments are required in order to ascertain the effect.

We have demonstrated that the use of Raman spectroscopy for quantifying damage in nanotube samples irradiated with high-energy ions can be ambiguous and lead to misleading conclusions on the sample structure after irradiation. This problem, related to non-uniform distribution of damage in the samples, is demonstrated experimentally for graphite and nanotube samples. This issue should carefully be taken into account when using Raman spectroscopy for characterizing damage in ion irradiated materials, and Raman probing depth should be compared to ion ranges when analyzing samples with a non-homogeneous distribution of defects. The TEM method probes the very surface layer where damage is also different from that in the bulk, and this further complicates the comparison of Raman and TEM results. Finally, other carbon nanosystems, such as graphitic crystallites and carbon onions, present in our nanotube samples that are usually outside the TEM analysis may strongly contribute to the Raman spectra.

Acknowledgments

We thank the Academy of Finland for support through several research projects and the Finnish Centre of Excellence in Computational Molecular Science for support. Support from Magnus Ehrnrooth Foundation, the FinNano Program (OPNA Consortium) and the University of Helsinki Research Funds (HENAKOTO) is also acknowledged.

References

[1] Jorio A, Dresselhaus G and Dresselhaus M S 2008 *Carbon Nanotubes: Advanced Topics in the Synthesis, Structure, Properties and Applications* (Berlin: Springer)

[2] Yu M-F, Lourie O, Dyer M J, Moloni K, Kelly T F and Ruoff R S 2000 Strength and breaking mechanism of multiwalled carbon nanotubes under tensile load *Science* **287** 637–40

[3] Zhang S, Mielke S L, Khare R, Troya D, Ruoff R S, Schatz G C and Belytschko T 2005 Mechanics of defects in carbon nanotubes: atomistic and multiscale simulations *Phys. Rev.* B **71** 115403

[4] Dumitrica T, Hua M and Yakobson B I 2006 Symmetry-, time-, and temperature-dependent strength of carbon nanotubes *Proc. Natl Acad. Sci. USA* **103** 6105–9

[5] Gómez-Navarro G, De Pablo P J, Gómez-Herrero J, Biel B, Garcia-Vidal F J, Rubio A and Flores F 2005 Tuning the conductance of single-walled carbon nanotubes by ion irradiation in the Anderson localization regime *Nat. Mater.* **4** 534–9

[6] Stahl H, Appenzeller J, Martel R, Avouris Ph and Lengeler B 2000 Intertube coupling in ropes of single-wall carbon nanotubes *Phys. Rev. Lett.* **85** 5186–9
[7] Ni Z, Ishaq A, Yan L, Gong J and Zhu D 2009 Enhanced electron field emission of carbon nanotubes by Si ion beam irradiation *J. Phys. D: Appl. Phys.* **42** 075408
[8] Kim D-H, Jang H-S, Kim C-D, Cho D-S, Kang H-D and Lee H-R 2003 Enhancement of the field emission of carbon nanotubes straightened by application of argon ion irradiation *Chem. Phys. Lett.* **378** 232–7
[9] Kis A, Csányi G, Salvetat J-P, Lee T-N, Couteau E, Kulik A J, Benoit W, Brugger J and Fórro L 2004 Reinforcement of single-walled carbon nanotube bundles by intertube bridging *Nat. Mater.* **3** 153–7
[10] Sammalkorpi M, Krasheninnikov A V, Kuronen A, Nordlund K and Kaski K 2005 Irradiation-induced stiffening of carbon nanotube bundles *Nucl. Instrum. Methods Phys. Res.* B **228** 142–5
[11] Peng B, Locascio M, Zapol P, Li S, Mielke S L, Schatz G C and Espinosa H D 2008 Measurements of near-ultimate strength for multiwalled carbon nanotubes and irradiation-induced crosslinking improvements *Nat. Nanotechnol.* **3** 626–31
[12] Skakalova V, Kaiser S and Roth A B 2008 Raman mode shifts correlated with conductivity and Young's modulus changes in modified carbon nanotube networks *Phys. Status Solidi RRL* **2** 62–4
[13] Skákalová V, Kaiser A B, Osváth Z, Vértesy G, Biró L P and Roth S 2008 Ion irradiation effects on conduction in single-wall carbon nanotube networks *Appl. Phys.* A **90** 597–602
[14] Åström J A, Krasheninnikov A V and Nordlund K 2004 Carbon nanotube mats and fibers with irradiation-improved mechanical characteristics: a theoretical model *Phys. Rev. Lett.* **93** 215503
[15] Krasheninnikov A V and Banhart F 2007 Engineering of nanostructured carbon materials with electron or ion beams *Nat. Mater.* **6** 723–33
[16] Krasheninnikov A V and Nordlund K 2010 Ion and electron irradiation-induced effects in nanostructured materials *J. Appl. Phys.* **107** 071301
[17] Banhart F and Ajayan P M 1996 Carbon onions as nanoscopic pressure cells for diamond formation *Nature* **382** 433–5
[18] Wesolowski P, Lyutovich Y, Banhart F, Carstanjen H D and Kronmüller H 1997 Formation of diamond in carbon onions under MeV ion irradiation *Appl. Phys. Lett.* **71** 1948–50
[19] Sun L, Krasheninnikov A V, Ahlgren T, Nordlund K and Banhart F 2008 Plastic deformation of single nanometer-sized crystals *Phys. Rev. Lett.* **101** 156101
[20] Sun L, Banhart F, Krasheninnikov A V, Rodríguez-Manzo J A, Terrones M and Ajayan P M 2006 Carbon nanotubes as high-pressure cylinders and nanoextruders *Science* **312** 1199–202
[21] Misra A, Tyagi P K, Singh M K, Misra D S, Ghatak J, Satyam P V and Avasthi D K 2006 Structural damage on multiwalled carbon nanotubes and encapsulated single crystal nickel nanorods irradiated with Au^{+7} ions of 100 MeV *Diam. Relat. Mater.* **15** 300–3
[22] Kumar A, Avasthi D K, Pivin J C and Koinkar P M 2008 Ordering of fullerene and carbon nanotube thin films under energetic ion impact *Appl. Phys. Lett.* **92** 221904
[23] Mikó C, Milas M, Seo J W, Couteau E, Barisić N, Gaál R and Forró L 2003 Effect of electron irradiation on the electrical properties of fibers of aligned single-walled carbon nanotubes *Appl. Phys. Lett.* **83** 4622–4
[24] Ishaq A, Yan L and Zhu D 2009 The electrical conductivity of carbon nanotube sheets by ion beam irradiation *Nucl. Instrum. Methods Phys. Res.* B **267** 1779–82
[25] Jorio A, Pimenta M A, Souza Filho A G, Saito R, Dresselhaus G and Dresselhaus M S 2003 Characterizing carbon nanotube samples with resonance Raman scattering *New J. Phys.* **5** 139
[26] Dresselhaus M S, Dresselhaus G, Saito R and Jorio A 2005 Raman spectroscopy of carbon nanotubes *Phys. Rep.* **409** 47–99
[27] Kalbac M, Hsieh Y-P, Farhat H, Kavan L, Hofmann M, Kong J and Dresselhaus M S 2010 Defects in individual semiconducting single wall carbon nanotubes: Raman spectroscopic and *in situ* Raman spectroelectrochemical study *Nano Lett.* **10** 4619–26
[28] Malola S, Häkkinen H and Koskinen P 2008 Raman spectra of single-walled carbon nanotubes with vacancies *Phys. Rev.* B **77** 155412

[29] Felten A, Gillon X, Gulas M, Pireaux J-J, Ke X, Van Tendeloo G, Bittencourt C, Najafi E and Hitchcock A P 2010 Measuring point defect density in individual carbon nanotubes using polarization-dependent x-ray microscopy *ACS Nano* **4** 4431–6

[30] Ni B, Andrews R, Jacques D, Qian D, Wijesundara M B J, Choi Y, Hanley L and Sinnott S B 2001 A combined computational and experimental study of ion-beam modification of carbon nanotube bundles *J. Phys. Chem.* B **105** 12719–25

[31] Yang D Q, Rochette J-F and Sacher E 2005 Controlled chemical functionalization of multiwalled carbon nanotubes by kiloelectronvolt argon ion treatment and air exposure *Langmuir* **21** 8539–45

[32] Morant C, Andrey J, Prieto P, Mendiola D, Sanz J M and Elizalde E 2006 XPS characterization of nitrogen-doped carbon nanotubes *Phys. Status Solidi* **203** 1069–75

[33] Beuneu F, L'Huillier C, Salvetat J-P, Bonard J-M and Forró L 1999 Modification of multiwall carbon nanotubes by electron irradiation: an ESR study *Phys. Rev.* B **59** 5945–9

[34] Adhikari A R, Huang M B, Bakhru H, Talapatra S, Ajayan P M and Ryu C Y 2006 Effects of proton irradiation on thermal stability of single-walled carbon nanotubes mat *Nucl. Instrum. Methods Phys. Res.* B **245** 431–4

[35] Lucchese M M, Stavale F, Ferreira E H M, Vilani C, Moutinho M V O, Capaz R B, Achete C A and Jorio A 2010 Quantifying ion-induced defects and Raman relaxation length in graphene *Carbon* **48** 1592–7

[36] Ferreira E H M, Moutinho M V O, Stavale F, Lucchese M M, Capaz R B, Achete C A and Jorio A 2010 Evolution of the Raman spectra from single-, few-, and many-layer graphene with increasing disorder *Phys. Rev.* B **82** 125429

[37] Tian Y, Jiang H, Pfaler J V, Zhu Z, Nasibulin A G, Nikitin T, Aitchison B, Khriachtchev L, Brown D P and Kauppinen E I 2010 Analysis of the size distribution of single-walled carbon nanotubes using optical absorption spectroscopy *J. Phys. Chem. Lett.* **1** 1143–8

[38] Jeong B W, Ihm J and Lee G-D 2008 Stability of dislocation defect with two pentagon–heptagon pairs in graphene *Phys. Rev.* B **78** 165403

[39] Krasheninnikov A V 2001 Predicted scanning microscopy images of carbon nanotubes with atomic vacancies *Solid State Commun.* **118** 361–5

[40] Krasheninnikov A V and Elesin V F 2000 The effect of interstitial clusters and vacancies on the STM image of graphite *Surf. Sci.* **454–456** 519–24

[41] Krasheninnikov A V, Nordlund K and Keinonen J 2002 Carbon nanotubes as masks against ion irradiation: an insight from atomistic simulations *Appl. Phys. Lett.* **81** 1101–3

[42] Appelhans D J, Carr L D and Lusk M T 2010 Embedded ribbons of graphene allotropes: an extended defect perspective *New J. Phys.* **12** 125006

[43] Lusk M T and Carr L D 2008 Nanoengineering defect structures on graphene *Phys. Rev. Lett.* **100** 175503

[44] Ziegler J F and Biersack J P 2008 *Program TRIM* http://www.srim.org

[45] Gan Y, Kotakoski J, Krasheninnikov A V, Nordlun K and Banhart F 2008 The diffusion of carbon atoms inside carbon nanotubes *New J. Phys.* **10** 023022

[46] Banhart F 1999 Irradiation effects in carbon nanostructures *Rep. Prog. Phys.* **62** 1181–21

[47] Krasheninnikov A V, Lehtinen P O, Foster A S and Nieminen R M 2006 Bending the rules: contrasting vacancy energetics and migration in graphite and carbon nanotubes *Chem. Phys. Lett.* **418** 132–6

[48] Krasheninnikov A V, Nordlund K, Lehtinen P O, Foster A S, Ayuela A and Nieminen R M 2004 Adsorption and migration of carbon adatoms on zigzag nanotubes *Carbon* **42** 1021–5

[49] Yuchen M 2007 Simulation of interstitial diffusion in graphite *Phys. Rev.* B **76** 075419

[50] Li L, Reich S and Robertson J 2005 Defect energies of graphite: density-functional calculations *Phys. Rev.* B **72** 184109

[51] Teobaldi G, Tanimura K and Shluger A L 2010 Structure and properties of surface and subsurface defects in graphite accounting for van der Waals and spin-polarization effects *Phys. Rev.* B **82** 174104

[52] Teobaldi T, Ohnishi H, Tanimura K and Shluger A L 2010 The effect of van der Waals interactions on the properties of intrinsic defects in graphite *Carbon* **48** 4145–61

[53] Telling R H, Ewels C P, El-Barbary A A and Heggie M I 2003 Wigner defects bridge the graphite gap *Nat. Mater.* **2** 333–7

[54] Tolvanen A, Kotakoski J, Krasheninnikov A V and Nordlund K 2007 Relative abundance of single and double vacancies in irradiated single-walled carbon nanotubes *Appl. Phys. Lett.* **91** 173109

[55] Lehtinen O, Kotakoski J, Krasheninnikov A V and Keinonen J 2011 Cutting and controlled modification of graphene with ion beams *Nanotechnology* **22** 175306

[56] Ziegler J F, Biersack J P and Ziegler M D 2008 *The Stopping and Range of Ions in Matter* (Chester, MD: SRIM)

[57] Komarov F F 2003 Defect and track formation in solids irradiated by superhigh-energy ions *Phys.—Usp.* **46** 1253–82

[58] Liu J, Neumann R, Trautmann C and Müller C 2001 Tracks of swift heavy ions in graphite studied by scanning tunneling microscopy *Phys. Rev.* B **64** 184115

[59] Caron M, Rothard H, Toulemonde M, Gervais B and Beuve M 2006 Theoretical and experimental study of electronic temperatures in heavy ion tracks from Auger electron spectra and thermal spike calculations *Nucl. Instrum. Methods Phys. Res.* B **245** 36–40

[60] Lehtinen O, Kotakoski J, Krasheninnikov A V, Tolvanen A, Nordlund K and Keinonen J 2010 Effects of ion bombardment on a two-dimensional target: atomistic simulations of graphene irradiation *Phys. Rev.* B **81** 153401

[61] Arndt A, Spoddig D, Esquinazi P, Barzola-Quiquia J, Dusari S and Butz T 2009 Electric carrier concentration in graphite: dependence of electrical resistivity and magnetoresistance on defect concentration *Phys. Rev.* B **80** 195402

[62] Itoh N, Duffy D M, Khakshouri S and Stoneham A M 2009 Making tracks: electronic excitation roles in forming swift heavy ion tracks *J. Phys.: Condens. Matter* **21** 474205

[63] Ferrari A C and Robertson J 2000 Interpretation of Raman spectra of disordered and amorphous carbon *Phys. Rev.* B **61** 14095–107

[64] Dresselhaus M S, Jorio A, Hofmann M, Dresselhaus G and Saito R 2010 Perspectives on carbon nanotubes and graphene Raman spectroscopy *Nano Lett.* **10** 751–8

[65] Sato K, Saito R, Oyama Y, Jiang J, Cancado L G, Pimenta M A, Jorio A, Samsonidze Ge G, Dresselhaus G and Dresselhaus M S 2006 D-band Raman intensity of graphitic materials as a function of laser energy and crystallite size *Chem. Phys. Lett.* **427** 117–21

[66] Khriachtchev L 2006 Raman spectroscopy and optical properties of amorphous diamond-like carbon films *Top. Appl. Phys.* **100** 403–21

[67] Mathew S, Bhatta U M, Ghatak J, Sekhar B R and Dev B N 2007 The effects of 2 MeV Ag ion irradiation on multiwalled carbon nanotubes *Carbon* **45** 2659–64

[68] Ni Z, Li Q, Yan L, Gong J and Zhu D 2008 Large-scale fabrication of carbon nanowire networks using kilo-electron-volt ion beam *Diam. Relat. Mater.* **17** 365–71

[69] Nichols J A, Saito H, Deck C and Bandaru P R 2007 Artificial introduction of defects into vertically aligned multiwalled carbon nanotube ensembles: application to electrochemical sensors *J. Appl. Phys.* **102** 064306

[70] Khriachtchev L, Räsänen M, Novikov S, Kilpela O and Sinkkonen J 1999 Raman scattering from very thin Si layers of Si/SiO_2 superlattices: Experimental evidence of structural modification in the 0.8–3.5 nm thickness region *J. Appl. Phys.* **86** 5601–8

[71] Williams M W and Arakawa E T 1972 Optical properties of glassy carbon from 0 to 82 eV *J. Appl. Phys.* **43** 3460–3